DOI: 10.13009/EUCASS2023-343
Aerospace Europe Conference 2023 – 10TH EUCASS – 9TH CEAS

Interactive optimization of fluidic injection for single expansion ramp nozzle based on a modified autoencoder

Yunjia Yang, Jiazhe Li, Runze Li, Yufei Zhang, Haixin Chen†
School of Aerospace Engineering, Tsinghua University
100084 Beijing, People's Republic of China
yangyj20@mails.tsinghua.edu.cn – chenhaixin@tsinghua.edu.cn
† Corresponding Author

Abstract
The single expansion ramp nozzle often experiences poor thrust performance at overexpansion conditions. Fluidic injection presents a promising solution to mitigate this issue, although there lacks an effective method to determine injection parameters under varying nozzle operating conditions. This paper presents a novel residual autoencoder surrogate model to fast calculate the pressure and temperature profiles on nozzle surfaces. Considering the characteristics of the nozzle flowfield, the model is designed to predict the difference between the profiles with and without the injection. This approach boosts the model's predictive accuracy by 20% and enhances its transferability. Furthermore, the gradient-based optimization algorithm is applied to the model to discern optimal injection parameters under eleven distinct nozzle operating conditions whose nozzle pressure ratios range from 12 to 40. The results indicate a successful increase in average thrust coefficients by 0.76%, demonstrating the effectiveness of the proposed approach.

1. Introduction

The single expansion ramp nozzle (SERN) is an important component for wide-speed-range aerospace vehicles [1]. It generates most of the engine thrust and is also critical to the vehicle's pitching moment [2]. Typically, the nozzle contour is designed for high-altitude and high-speed cruise flight conditions, where the exceptionally low ambient pressure induces a large design nozzle pressure ratio (NPR). To make the gas fully expand under such conditions, the nozzles of high-speed vehicles are designed with a large geometric area ratio (AR). However, when the nozzle operates at a lower NPR during acceleration and deceleration, the large AR may lead to overexpansion and compromised performance.

The fluidic injection is one of the most promising solutions to overexpansion thanks to its efficiency, robustness, and capability to integrate with the engine's secondary air system [3,4]. Numerous studies have been conducted since the early 2000s to examine how injection parameters, such as location, intensity, and injection angle, influence nozzle performance [3-6]. During the acceleration and deceleration process, the flight altitude and speed are changing constantly, causing the nozzle's operating conditions to change as well. As a result, the optimal injection parameters vary under different flight conditions. To optimize overall performance, these parameters should be collectively considered and optimized.

However, there is currently no practical method to design and optimize injection parameters under multiple nozzle conditions due to high computational demands. Although there are fast prediction tools for injection flowfields based on the method of characteristics (MOC) [7], they fail to accurately simulate the separation zone around the injection slot, a crucial factor affecting injection performance. Plus, the MOC is difficult to predict the wall temperature profile, which is important to guide the cooling design of the nozzle [8]. Therefore, the Reynold averaged Navier-Stokes (RANS) simulation is necessary to obtain injection performance for each nozzle operating condition, which will bring a serious computation burden to the multi-condition optimization.

DOI: 10.13009/EUCASS2023-343

In recent years, machine-learning-based flowfield prediction models have become useful tools to replace time-consuming RANS simulations in the optimization process [9-13]. They act as a surrogate model to provide a fast evaluation of sample performance and gradients for the optimization algorithm. Meanwhile, they differ from other surrogate models in that they can provide samples' flowfields during the optimization process, allowing designers to understand the optimization process and mechanism. The method has been proven to be effective for various optimization tasks but has not been applied to the optimization of a fluidic injection nozzle.

The present paper applies the state-of-art machine learning technique to predict nozzle injection flowfields and optimize injection parameters. The supersonic nature of the nozzle flowfield is considered to improve the machine-learning prediction model. Given that the injection predominantly influences the flowfield in the vicinity and downstream of the slot, the majority of the nozzle flowfield remains unaltered post-injection. Thus, a residual autoencoder is designed to predict the difference that the injection brings to the non-injection baseline flowfield. Considering that the mechanism of the injection is similar under different nozzle conditions and injection parameters, the model is expected to exhibit better accuracy and generalizability.

At the same time as the nozzle flowfields are predicted with the model, the gradients of injection parameters to nozzle performance can also be cheaply obtained through the network with a back-propagation algorithm. Then, the gradients are used in the sequential least squares programming method to find the best combination of injection parameters.

2. Theory analysis of fluidic injection

Many researchers have studied the fluidic injection method to improve the thrust of a SERN, and have gained some understanding of its mechanism [5,6]. Figure 1 depicts an over-expanded SERN with a fluidic injection at the cowl surface. The pressure profiles on the ramp and cowl surfaces of the SERN with and without the fluidic injection are also shown in Fig.1.

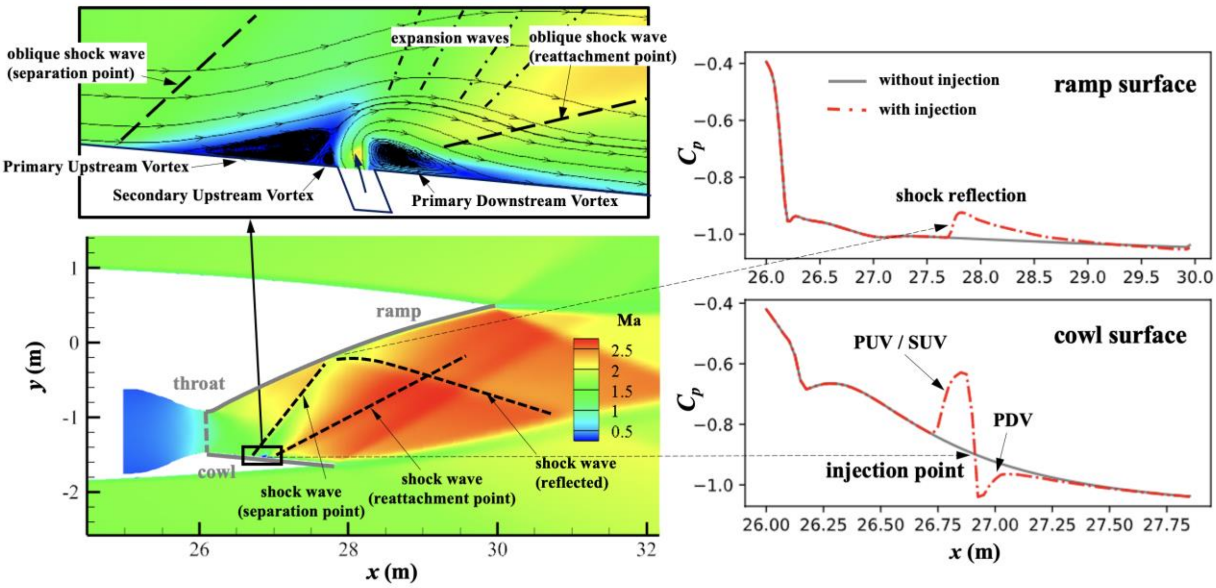

Figure 1: Flowfield and pressure profiles of a SERN with fluidic injection

As shown in Fig. 1, the injection forms a barrier against the mainstream, and a separation zone appears upstream of the injection. The separation consists of two vortices due to the shear stress, the primary upstream vortex (PUV) rotating clockwise and the secondary upstream vortex (SUV) rotating counterclockwise. The upstream vortex is like a wedge inserted into the mainstream, causing an oblique shock wave in front of the separation point. The shock wave deflects the mainstream and increases its pressure, forming a high-pressure zone on the cowl surface. Meanwhile, the shock wave propagates towards the opposite ramp surface and also forms a pressure peak on it. Then, the injection plume is forced to deflect and adhere to the wall, and during this process, expansion waves emerge in the mainstream. They gradually reduce the pressure peak formed by the shock wave when they hit the ramp. On the cowl surface, a clockwise rotating primary downstream vortex (PDV) is formed behind the slot, where the pressure is lower than the

DOI: 10.13009/EUCASS2023-343

baseline. At the end of the separation, the mainstream reattaches and another oblique shock wave occurs to turn the mainstream direction and restore the pressure.

The effect of fluidic injection on nozzle performance can be concluded into two aspects:

- The reaction force generated by the injection itself;
- The force generated by integrating the influence of injection on the wall pressure profile.

The two aspects of the effect can be analyzed quantitatively. The thrust generated by the nozzle can be expressed as the integral of the momentum flux through the throat and on the expansion wall surfaces:

$$\begin{aligned}\mathbf{F} &= \int_{A_8}\left[\rho\mathbf{V}(\mathbf{V}\cdot\mathbf{n})+(p-p_{\mathrm{atm}})\mathbf{n}\right]\mathrm{d}\Gamma + \int_{\mathrm{wall}}(p-p_{\mathrm{atm}})\mathbf{n}\,\mathrm{d}\Gamma \\ &= \mathbf{\Phi}_8 + \int_{\mathrm{wall}}(p-p_{\mathrm{atm}})\mathbf{n}\,\mathrm{d}\Gamma\end{aligned} \tag{1}$$

where $\mathbf{\Phi}_8$ is the momentum flux through the nozzle throat. Suppose the new pressure profile after introducing fluidic injection is p', and the new thrust is:

$$\mathbf{F}_{\mathrm{inj}} = \mathbf{\Phi}'_8 + \int_{\mathrm{wall}}(p'-p)\mathbf{n}\,\mathrm{d}\Gamma + \mathbf{\Phi}_{\mathrm{inj}} \tag{2}$$

where $\mathbf{\Phi}_{\mathrm{inj}}$ is the momentum flux through the injection slot. Since the injection won't influence upstream in a supersonic flowfield, we have $\mathbf{\Phi}'_8 = \mathbf{\Phi}_8$.

The x-direction thrust coefficient is used as the indicator of nozzle performance. For non-injection condition, it is defined as:

$$C_f = \frac{F_x}{F_{\mathrm{id}}} \tag{3}$$

The ideal thrust F_{id} can be derived as:

$$F_{\mathrm{id}} = m_8\sqrt{\frac{2\gamma RT_7^*}{\gamma-1}\left(1-\left(\frac{p_7^*}{p_{\mathrm{atm}}}\right)^{-\frac{\gamma-1}{\gamma}}\right)} \tag{4}$$

where m_8 is the mass flow rate through the throat, and p_7^*, T_7^* are the total pressure and temperature at the nozzle inlet.

For a nozzle with fluidic injection, the thrust coefficient is usually defined as:

$$C_{fx} = \frac{F_{\mathrm{inj},x}}{F_{\mathrm{id}} + F_{\mathrm{inj,id}}} \tag{5}$$

where $F_{\mathrm{inj,id}}$ is the ideal thrust of the fluidic injection which is calculated similarly to equation (4). From equations (1) and (2), it can be derived that if the injection effect is greater than the ideal thrust of the injection, i.e.,

$$F_{\mathrm{inj,id}} < \Delta F_x = \Phi'_{8,x} + \int_{\mathrm{wall}}(p'-p_{\mathrm{atm}})n_x\mathrm{d}\Gamma + \Phi_{\mathrm{inj},x} \tag{6}$$

Then, the fluidic injection will have a positive influence on the nozzle's performance.

DOI: 10.13009/EUCASS2023-343

3. Database establishment

In order to construct the machine-learning surrogate model for the flowfields of fluidic injection nozzles, a database has to be established to train the model in advance. The database contains flowfields with different nozzle conditions and injection parameters so that the trained model can be applied to optimization tasks with different nozzle conditions, thereby achieving the goal of interactive fast optimization. This section presents the sampling, calculation, and storage process of the database.

3.1. Sampling of nozzle and injection condition parameters

In the database, the geometry of the nozzle contour is fixed to a single ramp expansion nozzle designed for cruise Mach number Ma = 4.0 as shown in Fig. 2. The flight Mach number (Ma), flight height (H), nozzle pressure ratio (NPR), and total inlet temperature (T_7^*) are selected as the four parameters of the nozzle operating condition. Another four parameters are selected to describe the injection condition. They are the injection location (r), the injection angle (α), the secondary pressure ratio (SPR), and the total inlet temperature of the injection (T_s^*). The injection location is defined as the proportional station on the cowl flap surface, and the injection angle is defined as the angle between the injection and the tangent of the cowl flap surface. The SPR is defined as the ratio between injection total pressure and mainstream inlet total pressure. The slit width is fixed to 2 cm.

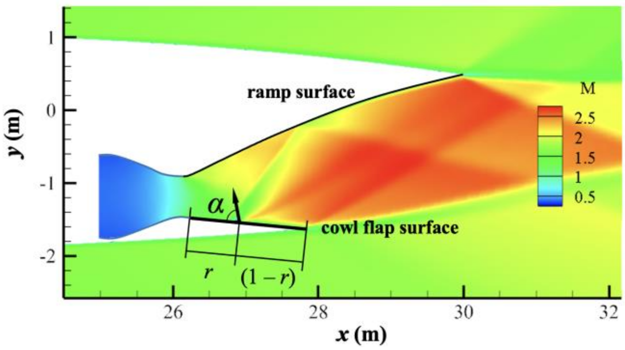

Figure 2: Nozzle geometry and the definition of the location and angle of the injection

The variation range of the eight nozzle and injection conditions are listed in Table. 1.

Table 1: Range of the nozzle and injection conditions

	***Nozzle operating conditions* (300)**				***Injection conditions* (300 ×24)**			
	Ma	***H***	**NPR**	T_7^*	***r***	α	***SPR***	T_s^*
lower boundary	1.5	15 km	3 + 6 × (Ma – 1.5)	900K	0.10	30 °	0.1	300
upper boundary	3.5	20 km	10 + 10 × (Ma – 1.5)	2000K	0.95	150 °	0.9	300 + 0.6 × (T_7^* – 1.5)

The Latin hypercube sampling (LHS) method [14] is used to generate 300 nozzle operating conditions. For each nozzle operating condition, 24 injection conditions are obtained with random uniform sampling. In total, there are 7200 groups of parameters in the database.

3.2. CFD methods

The CFD simulations are conducted to calculate the non-injection flowfields under the 300 nozzle operating conditions and flowfields with 24 injection conditions for each nozzle operating condition.

The two-dimensional, steady, and compressible Reynolds-averaged Navier–Stokes (RANS) equations are solved with the finite volume method. The total variation diminishing interpolation framework is used for spatial discretization, and the implicit scheme is used for time integration. The two-equation realizable k-ε model is used to model the

DOI: 10.13009/EUCASS2023-343

turbulence in the RANS equations. This model is commonly used for supersonic flow, especially secondary injection into a supersonic crossflow [15].

The simulations are conducted on the structured mesh. The inlet boundaries of the nozzle are specified with the given nozzle operating condition, and the boundaries for the external flow are determined by the characteristics of the Riemann invariants. The no-slip adiabatic condition is imposed on all the wall surfaces. The secondary flow passages are not included in the computation region, and the injection is introduced by applying the total pressure – total temperature boundary condition at the exit plane of the injection slot. The injection angle is set by imposing the velocity direction of the boundary condition. This method can reduce the mesh complexity and is used in a similar study [16].

The simulation methodology is validated based on the experimental data for a fluidic thrust vectoring two-dimensional nozzle contributed by Waithe and Deere [17]. In their study, the secondary injection is introduced in the divergent section on the upper nozzle surface, inducing oblique shock waves and flow separation. The simulation was conducted using three meshes with 16 thousand, 30 thousand, and 55 thousand cells. The wall pressure distributions on the upper surface for different meshes are depicted in Fig. 3 together with the experimental result obtained in Ref. [17]. It is demonstrated that the pressure distributions are similar despite the use of different meshes, indicating that the coarse mesh is sufficient for simulation.

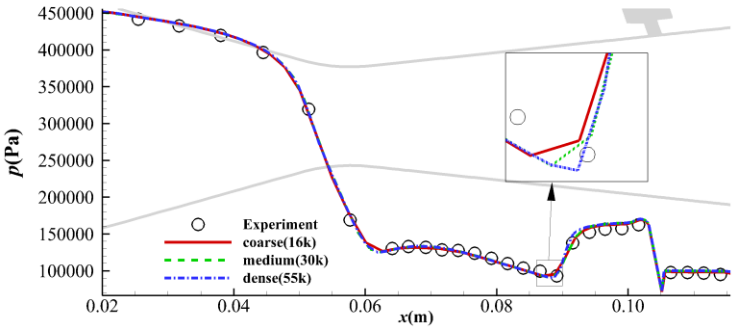

Figure 3: Upper surface wall pressure profiles with different mesh sizes

3.3. Postprocess

As mentioned in Section 2, the thrust coefficient of the nozzle can be obtained with the pressure profile (p) and the momentum flux through the nozzle throat ($\mathbf{\Phi}_8$). Meanwhile, the temperature profile (T) is important to guide the design of the cooling system. Therefore, the pressure, temperature profiles, and momentum flux through the nozzle throat are stored in the database and used in the following prediction model.

Since the injection locations are different among the samples, the meshes are different as well. To ensure the consistency of the data, the CFD simulated pressure and temperate fields are interpolated to a series of probe points on the ramp and cowl surfaces that is equidistant in the x-direction. Then these surface points are linked at the throat to form an array of 2 × 234, where the first dimension stands for the two flow variables, i.e., the pressure and the temperature, and the second dimension stands for the probe positions.

In addition, both the injection parameters and the profiles are converted to nondimensional for better training of the model. For the parameters, this is done with the upper and lower boundary of each parameter; while for the profiles, the total conditions at the nozzle inlet are used. The non-dimensional values can be written as:

$$\begin{aligned} \tilde{p} &= \frac{p_7^* - p}{p_7^* - p_{\mathrm{atm}}} = 1 - \frac{p / p_{\mathrm{atm}} - 1}{\mathrm{NPR} - 1} \\ \tilde{T} &= \frac{T_7^* - T}{T_7^* - T_{\mathrm{slit}}^*} \approx \eta \end{aligned} \tag{7}$$

DOI: 10.13009/EUCASS2023-343

4. Residual autoencoder model

This section presents the machine-learning-based prediction model for pressure and temperature profiles on the nozzle surface. The purpose is to generate the profiles under a given set of injection parameters and the non-injection profiles. The most straightforward approach involves directly predicting the injected profiles from the inputs, as depicted in Fig. 4 (a). However, due to the supersonic characteristics of the flowfield, a substantial part of the injection flowfield is the same as the non-injection flowfield. To account for this, we introduce a residual prediction model. This model is intended to predict the differences between the injection and non-injection profiles, as illustrated in Fig. 4 (b).

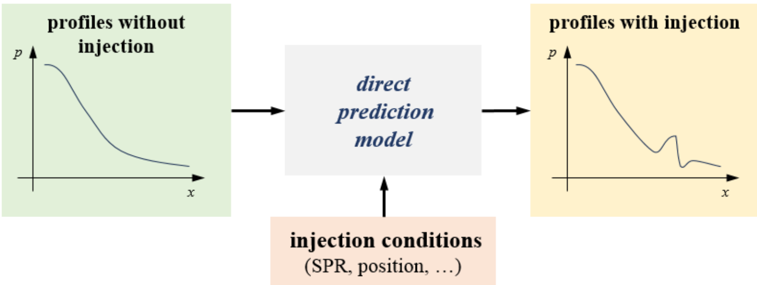

(a) Framework of the direct prediction model

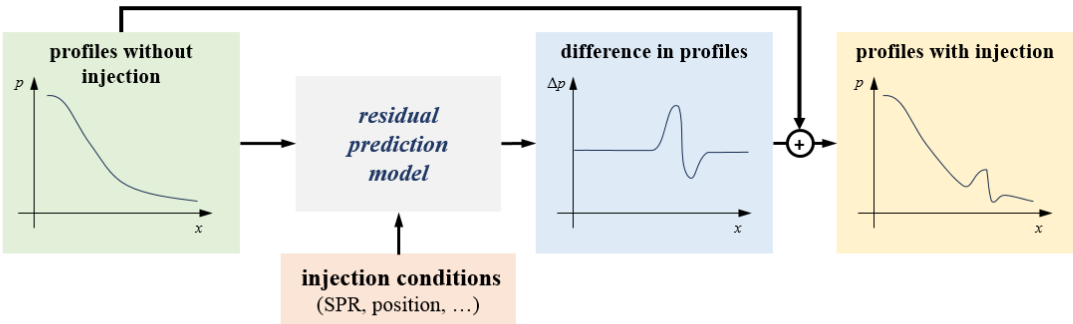

(b) Framework of the residual prediction model

Figure 4: Frameworks of the models

4.1. Model architecture

In the present paper, the residual prediction model is implemented with an autoencoder framework. Figure 5 describes the architecture of the residual autoencoder and the method to obtain the thrust coefficient. The model consists of two components: the encoder and the decoder. The encoder accepts the non-injection pressure and temperature profiles ($\tilde{p}, \tilde{T}$) as inputs, extracting a low-dimensional representation (***z***). The decoder then combines ***z*** with the injection parameters ($\tilde{r}, \tilde{\alpha}, \tilde{\mathrm{SPR}}, \tilde{T}_s^*$), generating the differences in the profiles ($\Delta\tilde{p}, \Delta\tilde{T}$). Then the differences are added to the non-injection profiles and get the pressure and temperature profiles under the given injection condition.

The one-dimensional convolution layers are utilized to construct both the encoder and the decoder. The encoder comprises three blocks of layers, each containing a 1D convolution layer with a kernel size (k) of 3 and a stride (s) of 2, as well as an average pooling layer with the same kernel size and stride. The channel amounts after each block are 32, 64, and 128, respectively. A densely connected layer then links the flattened output of the encoder to an 8-dimensional latent vector, ***z***. The decoder similarly consists of three blocks, each including a linear interpolation layer for up-sampling the 1D feature map and a convolution layer with a stride of 1. The channel amounts of each feature map are 512, 256, 128, and 128. The network concludes with another convolution layer with a stride of 1 to compress the last feature map to two channels. A LeakyReLU [18] function, with a slope of 0.2, is employed as the activation function. The network contains a total of 611 498 trainable parameters.

DOI: 10.13009/EUCASS2023-343

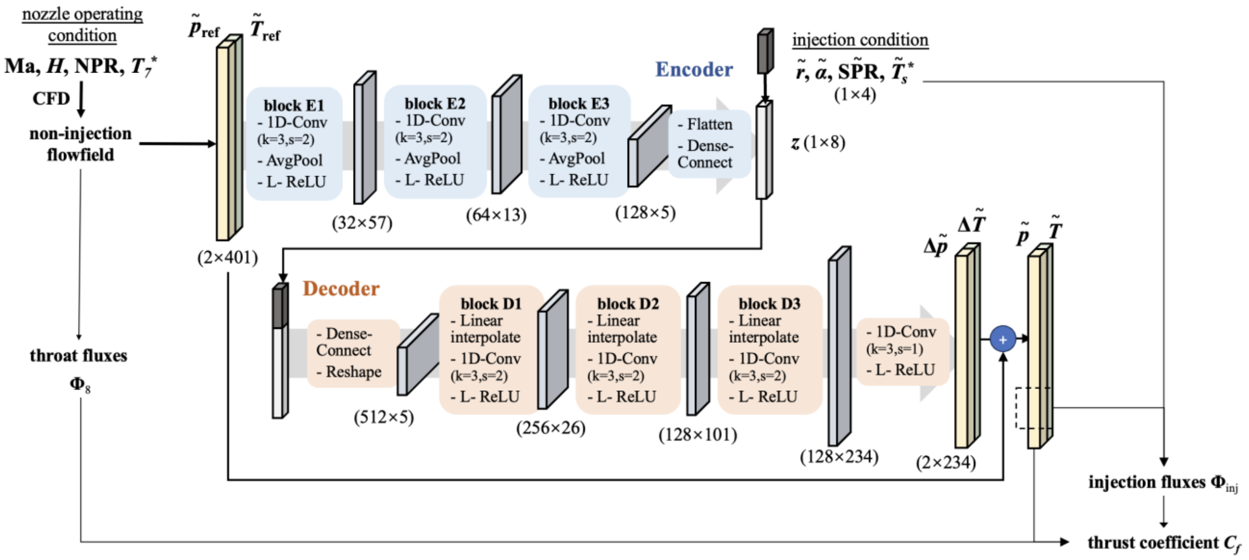

Figure 5: The architecture of the residual autoencoder and method to obtain thrust coefficient

There are several extra calculations to calculate the thrust coefficient (C_f) from the predicted profiles with equation (2). In the equation, the momentum flux through the throat ($\mathbf{\Phi}_8$), and the geometry values ($\mathbf{n}$, $\mathbf{\Gamma}$) can be directly obtained from the non-injection flowfield, while the x-directional momentum flux through the injection slot (Φ_{inj}) needs to be calculated from other variables with the isentropic relationship as follows:

$$\begin{aligned}
&\mathbf{\Phi}_{inj} = m_s V_s \\
&m_s = \sqrt{\frac{\gamma}{R}\left(1+\frac{\gamma-1}{2}\mathrm{Ma}_s^2\right)^{-\frac{\gamma+1}{\gamma-1}}}\cdot \mathrm{Ma}_s \cdot \frac{p_s^*}{\sqrt{T_s^*}} A_s \\
&V_s = \mathrm{Ma}_s \cdot \sqrt{\gamma R \cdot \frac{T_s^*}{1+\frac{\gamma-1}{2}\mathrm{Ma}_s^2}}
\end{aligned} \tag{8}$$

where $\mathrm{Ma_s}$ is the Mach number at the exit plane of the injection slot, and A_s is the exit plane area. They can be written as:

$$\begin{aligned}
&\mathrm{Ma}_s = \min\left[\sqrt{\frac{2}{\gamma-1}\left(\left(\frac{p_s^*}{p_s}\right)^{\frac{\gamma-1}{\gamma}}-1\right)}, 1.0\right] \\
&A_s = w\cdot \sin\alpha
\end{aligned} \tag{9}$$

In equations (8) to (9), the p_s^* and T_s^* are the total inlet condition of the injection. p_s is the static pressure at the exit plane, which is obtained by interpolation of the predicted pressure profile. w is the width of the slot, and α is the injection angle.

4.2. Training process

The aforementioned residual autoencoder is trained on the database established in Section 3. The database is divided into a training part and a testing part. The former contains the samples corresponding to 270 nozzle operating conditions, while the latter contains the other samples.

DOI: 10.13009/EUCASS2023-343

The loss function is selected to be the mean square error (MSE) between the model-predicted and CFD-simulated pressure and temperature profiles. The training hyperparameters are selected as follows. A fixed batch size of 16 is applied, and the Adam algorithm [19] is selected as the optimizer. The warmup strategy is employed to increase the learning rate from 5×10^{-5} in the first 20 epochs so that instability at the beginning of the training process can be avoided. Then the learning rate is reduced by an exponential function with a base of 0.95.

The training process is run three times to cross-validate the model. In each run, 10% of the samples are randomly selected from the training database as validation, and each run starts with random initialization of weights and biases in the model. During training, the losses on training and validation sets are monitored to avoid overfitting, and all three runs converge after 300 epochs.

4.3. Model performances

The model is tested on the samples corresponding to the 30 nozzle operating conditions in the testing database. For each testing nozzle operating condition, the non-injection flowfield is calculated with CFD and input into the residual prediction model. Then the pressure and temperature profiles under the 24 injection conditions are generated with the model and compared with the CFD-simulated results. The thrust coefficients can also be predicted with the model and are also compared.

To illustrate the advantage of the proposed residual model, a baseline model is set up to have the same backbone, but to directly predict the injection profiles rather than the difference. The best prediction performances of the two models on the testing database are shown in Table 2.

Table 2: Prediction errors of the direct and residual prediction model

	MSE of dimensionless pressure profiles	**MSE of dimensionless temperature profiles**	**Absolute errors of thrust coefficients**
direct prediction model	0.00240	0.00687	0.005%
residual prediction model	0.00192	0.00637	0.003%

It can be seen in Table 2 that the residual model reduces 20.0% and 7.2% of prediction errors for pressure and temperature profiles, respectively. It also raises the prediction accuracy of thrust coefficients by 0.002%. Figure 6 shows the predicted pressure and temperature profiles on the ramp and cowl surfaces of 12 randomly selected test samples. The colored dashed lines are profiles predicted with the model, and they match well with the CFD results that are shown in grey solid lines.

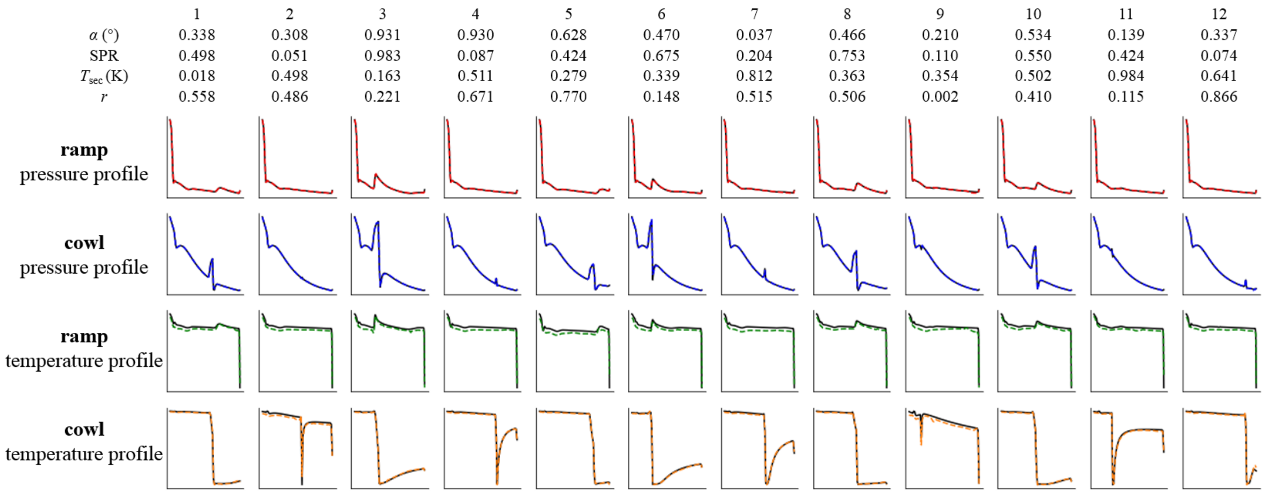

Figure 6: The residual-model-predicted and CFD-simulated pressure and temperature profiles

To further illustrate the advantage of the residual prediction model, it is tested in a double-slot case. In this case, two injection slots are located at r = 0.2 and r = 0.7. The upstream injection has an SPR = 0.5, T_s^* = 600K, and α = 90°,

DOI: 10.13009/EUCASS2023-343

while the downstream injection has an SPR = 0.7, $T_s^* = 400$K, and $\alpha = 90°$. The CFD-simulated flowfield is depicted in Fig. 7.

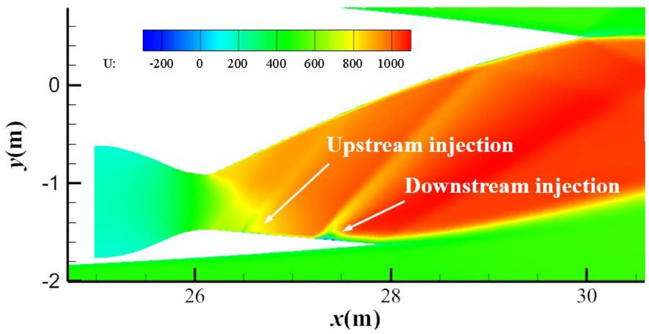

Figure 7: The flowfield of the double slot test case

The direct and residual prediction models are used to predict the pressure profiles of the double-injection case by calling the model twice during the prediction: for the first call, the non-injection profiles and the upstream injection conditions are input into the model; for the second call, the profiles output from the first call is input into the model again with the downstream injection conditions, generating the double-injection result.

Figure 8 illustrates the profiles predicted with the model. The results from the direct model are on the left, while the results of the residual model are on the right. The red and blue lines are the model-predicted results after the first and the second call, respectively, and the black line is the CFD-simulated ground truth.

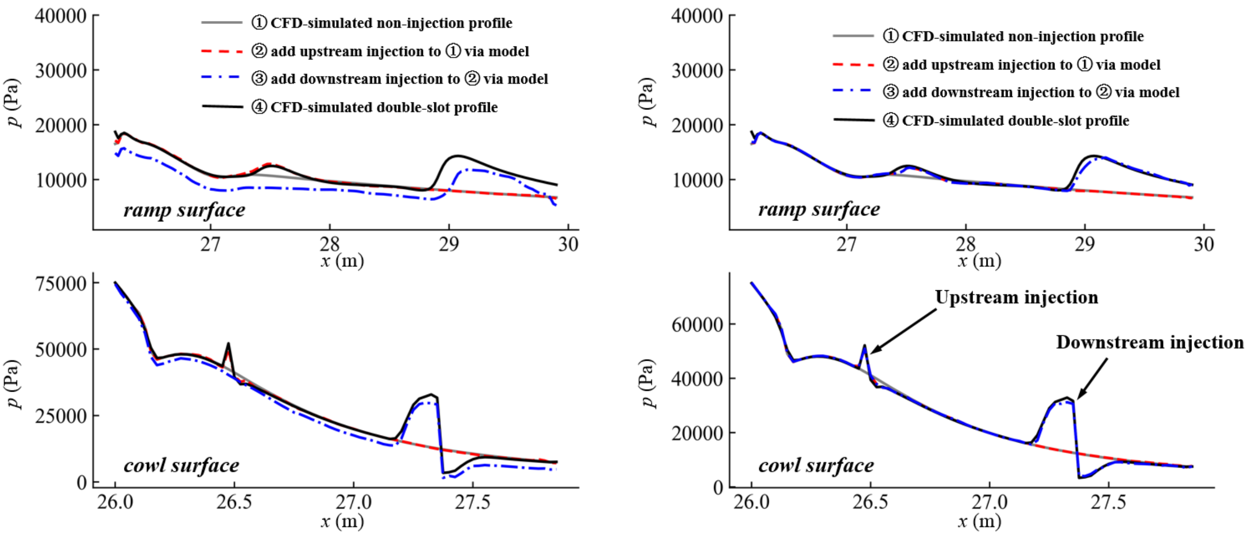

(a) pressure profiles predicted by the direct model (b) pressure profiles predicted by the residual model

Figure 8: Pressure profiles of the double-injection case on both surfaces

During training, all of the profiles input to the model are without injection, but in this case, the input profile (the red line) of the second call is different from those in the training process, since it is already influenced by one injection. In Fig.8 (a), the direct model failed to predict the double-injection profiles. It ignores the upstream injection and has an overall offset. However, in Fig.8 (b), the residual model manages to generate a reasonable result with correct pressure distribution.

It proves that the residual model can learn the influence region of an injection, and can neglect reluctant information in the input profiles. This guarantee that the residual model has a better transfer ability than the direct prediction model.

DOI: 10.13009/EUCASS2023-343

5. Model-based multi-condition optimization

As mentioned above, the fluidic injection offers a practical way to enhance SERN's performance under overexpansion. During acceleration and deceleration of the vehicle, the nozzle always works in a wide range of flow conditions, thus, it is important to optimize the injection parameters to seek a better overall nozzle performance under such conditions.

In the above study, a profile prediction model is constructed which can act as a surrogate model to give fast prediction of the nozzle pressure and temperature profiles with fluidic injection. With the help of the proposed model, it is possible to accomplish the multi-condition optimization within minutes when combining it with the gradient optimization algorithm.

5.1. Optimization methods

One of the advantages to use a surrogate model based on the neural network is that it can easily compute the gradients of the optimization objectives with respect to the design parameters [20]. It is realized via the back-propagation algorithm, which is the same way the model is trained.

The neural network consists of many differentiable functions that are connected to form a mapping function from input x (i.e., the injection condition parameters) to output f (i.e., the profiles and the thrust coefficients). The mapping function can be represented as $f = f(x; w)$ where w are the trainable weights and biases in the neural network. Since the network is formed with functions, it can be rewritten as:

$$f = \left(f_1 \circ f_2 \circ \cdots f_k \right)\left(x^0 \right) \tag{10}$$

where f_i is either a linear function or a non-linear activation function, which are combined to formulate the whole network. w_i are the trainable parameters corresponding to the function f_i. During the training process, the gradients of the loss function (error measure) L with respect to the parameters are computed using the chain rule:

$$\frac{\partial L}{\partial w_i} = \frac{\partial L}{\partial f} \dot{f}_k \cdots \dot{f}_{i+1} \dot{f}_i \tag{11}$$

The process is known as back-propagation. Then, these trainable parameters can be optimized to minimize the loss function. Once trained, the same back-propagation method can be used to compute the gradient of the optimization objective with respect to the design parameters as well. This process can be summarized as:

$$\frac{\partial J}{\partial x} = \frac{\partial J}{\partial f} \dot{f}_k \cdots \dot{f}_2 \dot{f}_1 \tag{12}$$

where $J = J(f)$ is the objective function, which is the averaged thrust coefficient in this case.

With the back-propagation algorithm, the gradients can be obtained fast and accurately. Therefore, in the present paper, the sequential least squares programming (SLSQP) method in the open-sourced SciPy library [21] is selected to utilize the back-propagated gradients to search the design space for the optimal injection parameters under multiple nozzle operating conditions.

5.2. Optimization setups

In order to have a better overall performance, eleven nozzle operating conditions are sampled through the flight envelope for joint optimization. Of the eleven conditions, the flight height and Mach number are evenly distributed from 15km to 20km, and from 2.5 to 3.5, respectively. The nozzle pressure ratio (NPR) and total inlet temperature are distributed from 12 to 40, and 1 200K to 1 448K, respectively.

For each nozzle operating condition, a CFD simulation is conducted to obtain the non-injection pressure and temperature profiles. These profiles serve as the input to the residual prediction model to calculate the injected profiles

DOI: 10.13009/EUCASS2023-343

and thrust coefficients when given the injection conditions under each nozzle operating condition. Then, the thrust coefficients under eleven nozzle operating conditions are averaged and recognized as the optimization objective.

The injection location, angle, inlet total temperature, and inlet pressure ratio are selected as the design parameters. Since it is difficult to change the injection's geometry configuration during flight, the injection location, angle, and inlet total temperature are fixed under the eleven operating conditions. In contrast, the injection's secondary pressure ratio is easier to be varied thanks to the secondary air system, so the SPRs for each . This gives a total of 14 design parameters. The framework of the optimization process is depicted in Fig. 9.

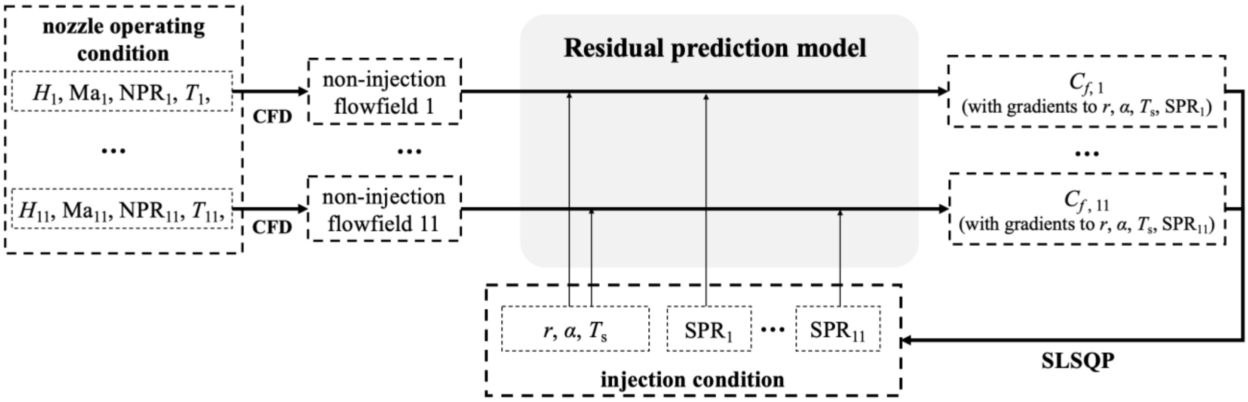

Figure 9: Framework of model-based multi-condition optimization

The design space of the injection parameters is the same as in Table 1. Due to the poor global searching capability of the gradient-based method, a multi-start method is adopted. 50 initial points are selected using the Latin hypercube sampling and optimizations are carried out from each point. The best results with the highest thrust coefficient will be chosen as the final result. In the optimization, if the initial injection intensity is small, the result will easily enter the local optimum where the injections tend to be eliminated. Therefore, the initial values of the SPRs are limited to greater than 0.5.

It is worth mentioning that further increasing the number of operating conditions will only lead to one more CFD simulation for each condition, and the time consumption for invoking the prediction model and the optimization algorithm is small.

5.3. Optimization results

Figure 10 depicts the optimization results for the best case among the multiple starts. The blue solid line indicates the thrust coefficients without injection of the eleven nozzle operating conditions, which is the baseline for the optimization. The orange solid line indicates the model-predicted thrust coefficients with the optimal injection parameters, and they are also verified with CFD which is shown as the black dashed line. The two lines are very close to each other, proving the effectiveness of the proposed residual prediction model. In this case, the averaged thrust coefficient is increased by 0.76%. Since the non-injection thrust coefficient is close to 1, achieving such optimization results within the range of NPRs in this optimization case is outstanding. The results also align with the conclusions given in other papers that study the injection parameters' influence [5,6].

DOI: 10.13009/EUCASS2023-343

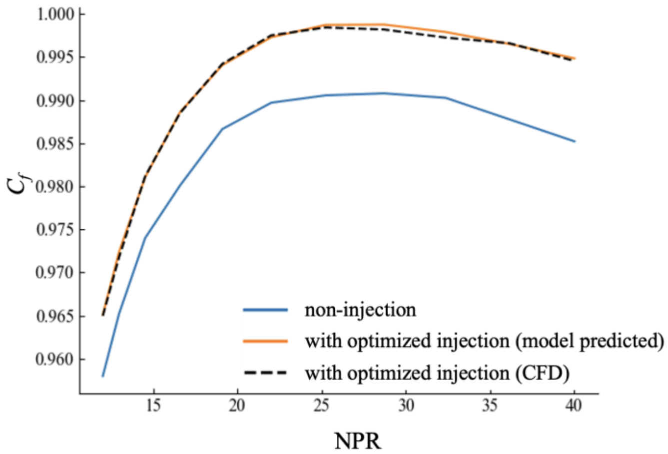

Figure 10: Optimization results for the thrust coefficients of eleven nozzle operating condition

Figure 11 shows the changes in the design variables during optimization. From Fig.11 (a), (c), and (d), it is indicated that the injection location, total inlet temperature, and the SPRs for all eleven operating conditions are optimized to the boundary. Since the excessive SPR may cause the nozzle thrust coefficient to decrease [5], it is probably because the upper boundary is too low to obtain the best injection performance.

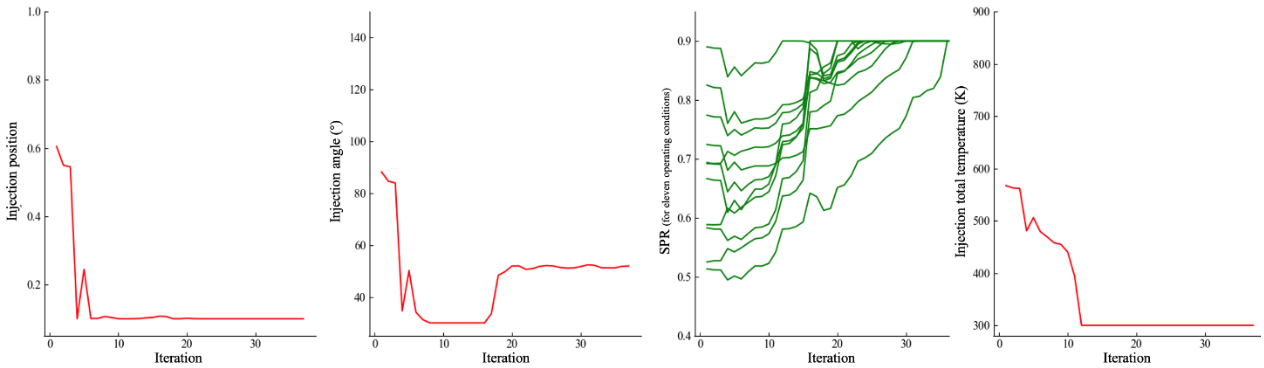

(a) Injection location (b) Injection angle (c) Injection SPRs (d) Injection total temperature

Figure 11: The design variables during optimization

In all, with the help of the residual autoencoder, the fluidic injection parameters under multiple nozzle operating conditions are optimized for the first time. The model is proven to be effective and efficient in optimization, and the proposed methodology can be easily applied to other optimization settings according to the engineering need.

6. Conclusion

Fluidic injection emerges as a promising solution to enhance the wide-speed-range performance of the single expansion ramp nozzle (SERN) system. This paper introduces a multi-condition interactive optimization method for injection parameters, leveraging cutting-edge neural network techniques. The key contributions of this study can be summarized as follows:

1) An innovative residual autoencoder that accounts for the nozzle flowfield characteristics is proposed. Given that fluidic injection only impacts the flowfield in proximity and downstream of the injection slot, our model is designed to predict the differences in pressure and temperature profiles with and without the injection. Compared to the direct prediction model, the proposed residual model reduces prediction errors for pressure and temperature profiles by 20.0% and 7.2%, respectively. The best prediction error for nozzle thrust coefficients is an impressively low 0.003%. Additionally, the model exhibits superior transferability to the double-slot test case.

DOI: 10.13009/EUCASS2023-343

2) The residual autoencoder is further employed in the multi-condition optimization for injection parameters. Trained on a database of 7500 nozzle flowfields under various nozzle operating conditions and injection conditions, the model is coupled with a gradient-based optimization method to identify optimal injection parameters under eleven different nozzle operating conditions within the flight envelope. The model can provide precise pressure and temperature profiles, along with the thrust coefficient, during the optimization process. Concurrently, the gradient of the objective with respect to design parameters is derived from the model using the back-propagation algorithm. The optimization process successfully increased average thrust coefficients by 0.76% across eleven nozzle operating conditions, with NPRs ranging from 12 to 40. The reliability of the model-predicted pressure and temperature profiles is confirmed via CFD.

Overall, this paper presents a practical methodology for optimizing nozzle thrust across multiple operating conditions. It illuminates potential applications of machine learning techniques in the design of aerospace propulsion systems, paving the way for future advancements in this field.

References

[1] Zheng Lv, Jinglei Xu, and Guangtao Song. 2019. “Design and Performance Analysis of an Exhaust System for an Over-under Turbine Based Combined Cycle Operating at Mach 0–6.” *Aerospace Science and Technology* 94 (November): 105386. https://doi.org/10.1016/j.ast.2019.105386.

[2] Edwards, C., W. Small, J. Weidner, and P. Johnston. 1975. “Studies of Scramjet/Airframe Integration Techniques for Hypersonic Aircraft.” In *13th Aerospace Sciences Meeting*. Pasadena, CA, U.S.A.: American Institute of Aeronautics and Astronautics. https://doi.org/10.2514/6.1975-58.

[3] Eric Gamble, Rich DeFrancesco, Dan Haid, and David Buckwalter. 2005. "Fluidic Nozzle to Improve Transonic Pitch and Thrust Performance of Hypersonic Vehicle." In *41st AIAA/ASME/SAE/ASEE Joint Propulsion Conference & Exhibit*. Tucson, Arizona: American Institute of Aeronautics and Astronautics. https://doi.org/10.2514/6.2005-3501.

[4] Yunjia Yang, Yufei Zhang, and Haixin Chen. 2023. “Analysis and Manipulation of the Separation Zone in an Overexpanded Combined Exhaust Nozzle.” *Aerospace Science and Technology* 135 (April): 108196. https://doi.org/10.1016/j.ast.2023.108196.

[5] Zheng Lv, Jinglei Xu, and Jianwei Mo. 2017. "Numerical Investigation of Improving the Performance of a Single Expansion Ramp Nozzle at Off-Design Conditions by Secondary Injection." *Acta Astronautica* 133 (April): 233-43. https://doi.org/10.1016/j.actaastro.2017.01.013.

[6] Gopinath Shanmugaraj, J V Muruga Lal Jeyan, and Vijay Kumar Singh. 2020. "Effects of Secondary Injection on the Performance of Over-Expanded Single Expansion Ramp Nozzle." *Journal of Physics: Conference Series* 1473 (1): 012002. https://doi.org/10.1088/1742-6596/1473/1/012002.

[7] Ing Chang, and Louis Hunter. 1994. “Over-under Nozzle CFD Study and Comparison with Data.” In *30th Joint Propulsion Conference and Exhibit*. Indianapolis,IN,U.S.A.: American Institute of Aeronautics and Astronautics. https://doi.org/10.2514/6.1994-2949.

[8] Yiwei Dong, Ertai Wang, Yancheng You, Chunping Yin, and Zongpu Wu. 2019. “Thermal Protection System and Thermal Management for Combined-Cycle Engine: Review and Prospects.” *Energies* 12 (2): 240. https://doi.org/10.3390/en12020240.

[9] Cihat Duru, Hande Alemdar, and Ozgur Ugras Baran. "A Deep Learning Approach for the Transonic Flowfield Predictions around Airfoils." Computers & Fluids 236 (2022): 105312. https://doi.org/10.1016/j.compfluid.2022.105312.

[10] Nils Thuerey, Konstantin Weienow, Lukas Prantl, and Xiangyu Hu. "Deep Learning Methods for Reynolds-Averaged Navier-Stokes Simulations of Airfoil Flows." AIAA Journal 58, no. 1 (January 2020): 25-36. https://doi.org/10.2514/1.J058291.

[11] Jing Wang, Cheng He, Runze Li, Haixin Chen, Chen Zhai, and Miao Zhang. "Flowfield Prediction of Supercritical Airfoils via Variational Autoencoder Based Deep Learning Framework." Physics of Fluids 33, no. 8 (August 2021): 086108. https://doi.org/10.1063/5.0053979.

DOI: 10.13009/EUCASS2023-343

[12] Haizhou Wu, Xuejun Liu, Wei An, and Hongqiang Lyu. "A Generative Deep Learning Framework for Airfoil Flowfield Prediction with Sparse Data." Chinese Journal of Aeronautics 35, no. 1 (January 2022): 470-84. https://doi.org/10.1016/j.cja.2021.02.012.

[13] Yunjia Yang, Runze Li, Yufei Zhang, and Haixin Chen. 2022. “Flowfield Prediction of Airfoil Off-Design Conditions Based on a Modified Variational Autoencoder.” AIAA Journal 60 (10): 5805–20. https://doi.org/10.2514/1.J061972.

[14] M. D. Mckay, R. J. Beckman, and W. J. Conover. 2000. “A Comparison of Three Methods for Selecting Values of Input Variables in the Analysis of Output From a Computer Code.” *Technometrics* 42 (1): 55–61. https://doi.org/10.1080/00401706.2000.10485979.

[15] Wei Huang, Wei-dong Liu, Shi-bin Li, Zhi-xun Xia, Jun Liu, Zhen-guo Wang, Influences of the turbulence model and the slot width on the transverse slot injection flow field in supersonic flows, *Acta Astronaut*. 73 (2012) 1–9, https:// doi.org/10.1016/j.actaastro.2011.12.003.

[16] Zhen Wang, Chongwen Jiang, Zhenxun Gao, Chunhian Lee, Prediction for the separation length of two-dimensional sonic injection with high-speed crossflow, *AIAA Journal*. 55 (3) (2017) 832–847, https://doi.org/10.2514/1.J055194.

[17] Kenrick Waithe, Karen Deere, An experimental and computational investigation of multiple injection ports in a convergent-divergent nozzle for fluidic thrust vectoring, in *21st AIAA Applied Aerodynamics Conference*, American Institute of Aeronautics and Astronautics, Orlando, Florida, 2003.

[18] Arun Kumar Dubey, and Vanita Jain. "Comparative Study of Convolution Neural Network's Relu and Leaky-Relu Activation Functions." In *Applications of Computing, Automation and Wireless Systems in Electrical Engineering*, edited by Sukumar Mishra, Yog Raj Sood, and Anuradha Tomar, 873-80. Singapore: Springer Singapore, 2019.

[19] Diederik P. Kingma, and Jimmy Ba. "Adam: A Method for Stochastic Optimization." *ArXiv*:1412.6980 [Cs], January 29, 2017. http://arxiv.org/abs/1412.6980.

[20] S. Ashwin Renganathan, Romit Maulik, and Jai Ahuja. 2021. “Enhanced Data Efficiency Using Deep Neural Networks and Gaussian Processes for Aerodynamic Design Optimization.” *Aerospace Science and Technology* 111 (April): 106522. https://doi.org/10.1016/j.ast.2021.106522.

[21] Pauli Virtanen, Ralf Gommers, Travis E. Oliphant, Matt Haberland, Tyler Reddy, David Cournapeau, Evgeni Burovski, et al. 2020. “SciPy 1.0: Fundamental Algorithms for Scientific Computing in Python.” *Nature Methods* 17: 261–72. https://doi.org/10.1038/s41592-019-0686-2.